Interfacial Structures Associated with Surface Activity in Magnetic Devitrified Glasses for Biomedical Applications

Interfacial Structures Associated with Surface Activity in Magnetic Devitrified Glasses for Biomedical Applications

Kiminori Sato[1], Enrica Vernè[2*], Marta Miola[2]

[1] Department of Environmental Sciences, Tokyo Gakugei University, Koganei, Tokyo 184-8501, Japan

[2] Politecnico di Torino, Applied Science and Technology Department, Corso Duca degli Abruzzi 24, 10129 Torino, Italy

* Corresponding author: sato-k@u-gakugei.ac.jp

Abstract

In bioactive devitrified glasses, the glass region with angstrom-scale open spaces reduces in comparison with relevant glass materials due to the formation of crystalline phases, e.g., magnetite-based crystals in ferrimagnetic devitrified glasses, thus deteriorating the bioactive properties arising from active surface area. This work aims to study the influence of a crystalline phase and the introduction, through different processes, of Cu ions, alternative to open spaces in the glass matrix, for Cu-loaded ferrimagnetic devitrified glasses by means of element-specific positronic studies coupled with other microscopic techniques. Cu ions, introduced by melt-quenching or ion-exchange process, are found to preferentially separate the magnetite-based crystals during synthesis by melt and quenching route increasing the concentration of crystal boundaries involved with the void-like open spaces. An interior surface of the void-like open spaces in the crystal boundaries contributes to the formation of carbonate species through the reaction of Ca with CO_2 in air evidencing surface activity.

Keywords

Magnetic materials; copper doping; open space; positron.

1. Introduction

Bioactive glasses and glass-ceramics have been widely explored for their ability to regenerate both hard and soft tissues [1,2]; moreover, their revolutionary role in cancer treatment was also recently explored [3-5]. In the last years, the researchers focused their attention on improving the biological activity of glasses/glass-ceramics by developing new formulations containing active elements (e.g. Cu, Ag, Zn, Mn, Sr, B and recently Te) [6-8] or second phases (e.g. magnetite, useful for hyperthermia treatment of tumors) [4,5] able to stimulate the genetic activation of specific cell and tissue pathways.

The improvement of materials functionalities can be achieved in different ways: i) introducing ions with therapeutic effects in their composition [9], ii) modifying the materials surfaces (e.g. by ion-exchange) [10], iii) promoting the nucleation of second phases/nanoparticles [11]. All these actions could introduce structural modification from micro to nano/pico level (e.g., defect presence); in particular, the introduction of an element in materials composition can affect the pores, the defect distribution and the chemical environment [12]. Active elements can be introduced by employing the conventional synthesis approach such as melt-quenching [13], the sol-gel method [14], and the ion exchanging [15], a technique specifically designed to introduce elements with an antibacterial effect. The emergence mechanism of antibacterial effect arising from these elements in bioactive glasses is, however, complex thus not being well understood yet. Furthermore, the introduction of these elements often causes a variation in the kinetics of the bioactivity mechanism. For example, it has been observed that Cu elements in bioactive glasses can cause bioactivity decrease if introduced as reagents in the melt and quenching process [16]. While it has been reported that by introducing Cu ions by the sol-gel method less influence on bioactivity is observed [15]. It is also reported that the reactivity of bioactive glasses depends on their composition and chemical/physical treatments [11]. In addition to the local state of loaded elements, the bioactive property seems to be associated with the surface properties [17]and the high specific surface area of the glass matrix with the high concentration of open spaces, as demonstrated for mesoporous glass scaffolds [18]. It is thus preferable to gain knowledge as to how active elements enter into host materials and induce the concomitant structural variation of local atomic sites, e.g. grain boundary.

A positively charged positron tends to localize in a nanoscale point defect as vacancy-like nano-defect in metals, in which a positively charged atomic nucleus is missing. The localized positrons are finally annihilated with electrons yielding two γ rays in opposite directions that provide information on the size of point defect and its chemical environment. This spectroscopic technique called as element-specific positron annihilation spectroscopy has given satisfactory results to probe locally disordered sites, as e.g., vacancy-sized free volume [18], grain boundary [19], polar element [20], nanoprecipitate [21], and local structural disorder [22], but it has not yet been investigated in bioactive glasses and glass ceramics. As a positron is the antiparticle of electron, the local space charge in the oxide ceramics can be identified as well [23, 24], which anticipates in specifying the local state of introduced Cu, e.g., ion or neutral atom.

In this work, a bioactive and ferrimagnetic devitrified glass (SC45), previously investigated for the hyperthermic treatment of tumors, was doped with copper, to confer antimicrobial properties, in two different ways: introducing copper as starting reactant or via an ion-exchange process in molten salts. It is reasonably inferred that the concentration of angstrom-scale open spaces decreases for the devitrified glasses due to the reduction of glass region deteriorating surface activity. The objective of this work is to focus on the alternative atomic sites exhibiting surface activity employing element-specific positron annihilation spectroscopy, addressing the mechanism of Cu accommodation into the boundaries among magnetite-based particles, and highlighting the surface activity of void-like open spaces found utilising positrons.

2. Materials and Methods

2.1 Synthesis of materials

A devitrified glass belonging to the system 24.7% SiO_2-13.5% CaO-13.5% Na_2O-3.3% P_2O_5-31% Fe_2O_3-14% (wt%) FeO (SC45) was produced using melt and quenching process as described in previous papers [25-28]. Briefly, the reactants were mixed and melted in a Pt crucible at 1550 °C for 30 minutes; the melt was poured into a brass mold to obtain bars, that were annealed at 600 °C for 12 hours, cut in slices of about 10x10x2 mm and polished with SiC abrasive papers, up to 1200 grit. The SC45 contains magnetite as crystalline phase

and has been completely characterized in terms of morphology, structure, composition, bioactivity, magnetic properties and biological behaviour in previous papers [25-28].

Subsequently, the SC45 was doped with copper with two different methods: on one hand, the composition was modified by introducing 5 wt% of CuO by replacing CaO (SC45-5Cu) during the melt and quenching process, as reported in [30]. On the other, SC45 was subjected to an ion-exchange process in $NaNO_3$ and $Cu(NO_3)_2$ molten salts, using a molar ratio between $NaNO_3/Cu(NO_3)_2$ of 20 (SC45-CuIE) [31]. SC45 slices were placed between two layers of salts, in a silica crucible, and heated at 380 °C for 30 minutes. At the end of the process, the samples were washed with bi-distilled water three times and dried at room temperature.

Since the SC45 contains SiO_2, CaO, Na_2O and P_2O_5 in the same ratio as the bioactive glass 45S5 (Bioglass®)[32], the 45S5 bioactive glass (45 SiO_2, 24.5 CaO, 24.5 Na_2O and 6.0 P_2O_5 wt%) was used as a control material. The 45S5 glass was produced by means of melt and quenching process as previously described.

2.2 Materials characterization

2.2.1 Morphological and structural characterization

The morphology of SC45 undoped and doped with copper was investigated using field emission scanning electron microscopy (FE-SEM, SUPRATM 40, Zeiss, Germany). For FE-SEM analysis samples were placed on aluminum stubs and coated with a thin chromium layer.

X-Ray diffraction analysis was performed to evaluate the structure of the samples, and to verify the presence of magnetite and the eventual formation of other crystalline phases due to the copper introduction. X-Ray diffraction was performed in the 2θ angle range from 10° to 70° with a scan rate of 4°/min, using Cu-Kα diffractometer (Ultima IV, RIGAKU, Japan). The acquired spectra were compared with previous works [30,31] using the "X'Pert High Score" program, with the PCPDFWIN database (2002 JCPDS- International Centre for Diffraction Data).

2.2.2. Positron annihilation spectroscopy

As mentioned above, positron annihilation spectroscopy is known as a powerful tool for examining the detailed structure of open spaces in materials. This element-specific spectroscopic technique is generally conducted by positron lifetime spectroscopy coupled with coincident Doppler broadening (CDB)

spectroscopy. Positron lifetime spectroscopy was performed at room temperature. The positron source (^{22}Na), sealed in a thin foil of Kapton, was mounted in a sample-source-sample sandwich for the measurements. Positron lifetime spectra (~1 × 10^6 coincidence counts) were recorded with a digital oscilloscope-based spectrometer, where the time resolution of 200 ps full-width at half-maximum was achieved. The validity of our lifetime measurements and data analysis was confirmed with certified reference materials (NMIJ CRM 5601-a and 5602-a) provided by the National Metrology Institute of Japan, and the National Institute of Advanced Industrial Science and Technology [33, 34]. In CDB spectroscopy, the energies of two annihilation quanta E_1 and E_2 were measured with a collinear set-up of two high-purity Ge detectors. The spectra were obtained by cutting the E_1, E_2 spectra along the energy conservation line $E_1 + E_2 = (1022 \pm 1)$ keV, taking into account the annihilation events within a strip of ± 1.6 keV.

2.2.3 Electrochemical impedance spectroscopy

Electrochemical impedance spectroscopy was conducted at room temperature using the impedance module of SP-150 (Biologic, France). The frequency range was 100 mHz–100 kHz with an alternative voltage amplitude of 10 mV. The measured impedance data were analyzed with an equivalent electrical circuit using Z-View software (Scribner Associates Inc., USA).

2.2.4 FT-IR spectroscopy

Attenuated total reflection (ATR) FT-IR spectra were measured using a Nicolet iS5 FT-IR spectrometer (Thermo Fisher Scientific Inc., USA) equipped with an ATR device and diamond crystal plate. All FT-IR spectra were measured at room temperature with a resolution of 4 cm^{-1}. The measurements were repeated 100 times to improve the statistical accuracy. The final spectra were obtained by averaging them. The software OMNIC 8.2 was used to display absorbance spectra by converting ATR data.

Results and Discussion

The morphology of the obtained materials, and in particular the possible influence of the copper introduction, was evaluated by means of FE-SEM analysis. Figure 1 displays the microstructures of SC45, SC45-5Cu and SC45-CuIE; as already evidenced in previous works [28, 30], SC45 sample (Figure 1 a, b, and c) shows the presence of elongated columns of octahedral crystals of magnetite (face-centred cubic inverse

spinel structure). The SC45-Cu sample (Figure 1 d, e, and f) shows the same crystals embedded in the glassy matrix, together with distorted magnetite crystals; as already discussed [30, 35] and observed in this work, the introduced copper (about 2.3 at%, slightly lower than the theoretical one) enters into the magnetite unit cell, modifying the structure of the crystals, and is also present in the boundaries between crystallite-crystallite interfaces. While the use of the ion-exchange technique (Figure 1 g, h, and i) allows to introduce copper (about 1.1 at %, EDS analysis not reported) without affecting the structure of magnetite crystals. The analysis of SC45-CuIE shows only a rougher surface due to the exchange process.

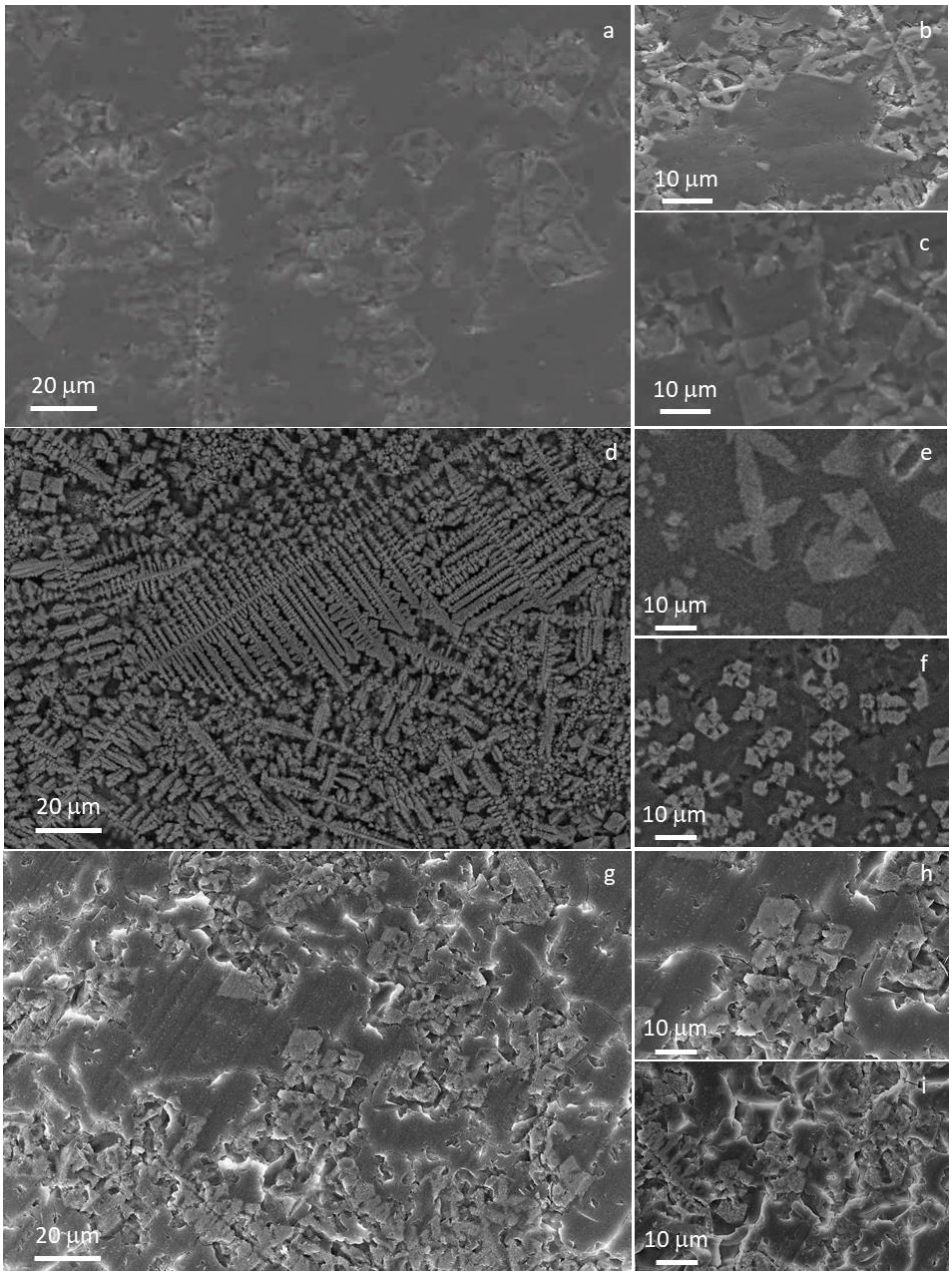

Figure 1: FE-SEM images of a SC45 a) magnification 2kx, b) and c) magnification 5kx; SC45-%Cu d) magnification 2kx, e) and f) magnification 5kx; SC45-CuIE g) magnification 2kx, h) and i) magnification 5kx.

Figure 2 shows XRD patterns for 45S5 glass and devitrified glasses (SC45, SC45-5Cu, and SC45-CuIE). The diffraction pattern of 45S5 glass is of typical amorphous phase.

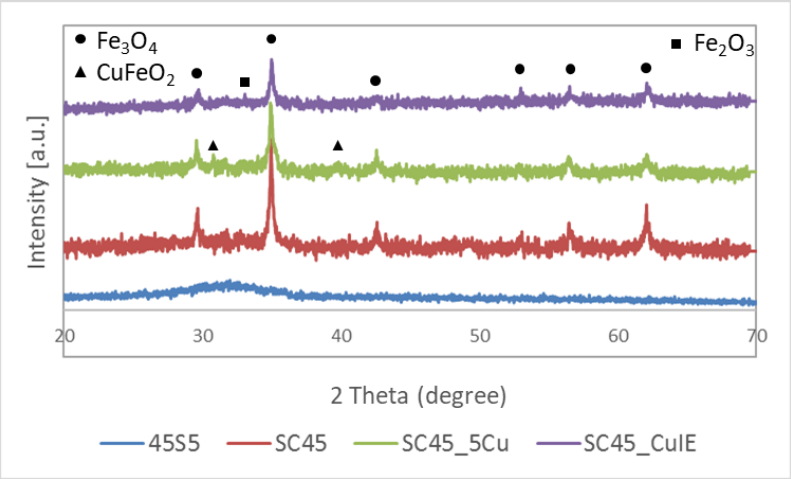

Figure 2: XRD patterns of 45S5 glass, SC45 and Cu-doped SC45.

On the other hand, the SC45, SC45-5Cu, and SC45-CuIE exhibit the peaks arising from the formation of magnetite phases in consistency with the results of FE-SEM observation, and a small amount of hematite (2 Theta = 33.2°, ref. code 01-073-0603). The tiny peak of copper iron oxide phase ($CuFeO_2$) is found for SC45-5Cu, in accordance with the previous studies (2 Theta = 31.3° and 40.2°, ref. code 01-074-1953) [30]. The peak of the magnetite phase for SC45-5Cu is broader than that of SC45, indicating that the crystallite size of magnetite for SC45-5Cu is smaller than that of SC45. The peak broadening of magnetite proceeds together with the disappearance of some relevant peaks for SC45-CuIE, enhancing the shrinkage of magnetite crystallites. The average sizes of magnetite crystallite evaluated from the (220) peak broadening employing Scherrer's formula are listed in Table I, in which the magnetite crystallite sizes are SC45 > SC45-5Cu > SC45-CuIE. Presumably Cu ions, introduced using the melt and quenching process (SC45-5Cu), are located at interfaces between magnetite crystallites interfering with their growth, as observed by FE-SEM analysis. The presence of Cu ions at the crystallite-crystallite interfaces will be discussed more in detail based on the results of element-specific positron annihilation spectroscopy later. The small crystallite size for SC45-CuIE could be associated with the mild annealing condition in comparison with that of SC45-5Cu.

Table I: Crystallite sizes of magnetite and conductivities for (a) 45S5, (b) SC45, (c) SC45-5Cu, and (d) SC45-CuIE.

sample	crystallite size [nm]	conductivity [S cm^{-1}]
(a) 45S5	--	3.6×10^{-7}
(b) SC45	34	1.2×10^{-7}
(c) SC45-5Cu	31	1.0×10^{-7}
(d) SC45-CuIE	23	9.5×10^{-8}

Figure 3 shows the result of electrochemical impedance spectroscopy for (a) 45S5, (b) SC45, (c) SC45-5Cu, and (d) SC45-CuIE, where the negative of the imaginary versus the real parts of the complex impedance referred to as Nyquist plots are presented.

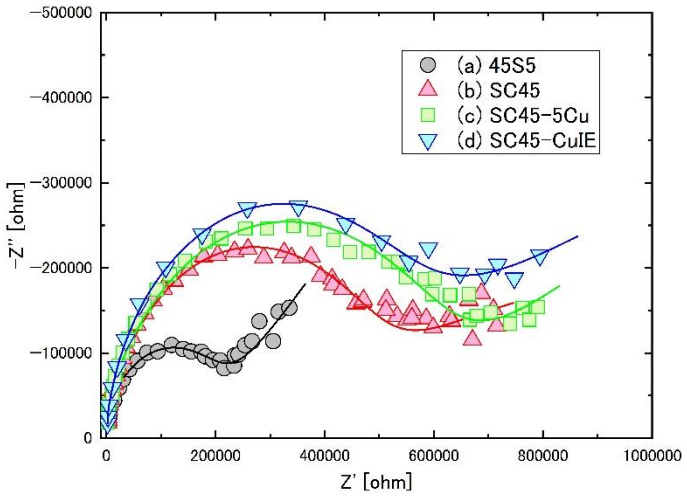

Figure 3: Nyquist plots for (a) 45S5 (black circles), (b) SC45 (red triangles), (c) SC45-5Cu (green squares), and (d) SC45-CuIE (blue inverse squares). The solid lines are the results of the fits employing two-equivalent circuit model.

Semi-circles appear in the Nyquist plots for all the samples, which is caused by ionic mobility generally higher than that of localized electrons in glass and devitrified materials. The solid lines in Figure 3 are the results of the fits employing a two-equivalent circuit model, in which ionic conductivities of the order of ~10^{-7} S cm^{-1} are evaluated (see Table I). The evaluated ionic conductivities are similar to those reported for other 45S5 glasses [36]. The 45S5 glass with an amorphous structure has the highest concentration of free volumes being tortuous open spaces, in which Na^{+}, added as a network modifier, participates in conductivity with 3.6×10^{-7}

S cm^{-1}. The semi-circle of SC45 is larger than that of 45S5 glass, decreasing the conductivity down to 1.2×10^{-7} S cm^{-1}. As observed in the FE-SEM and XRD analysis, SC45 sample revealed the largest fraction of magnetite-based particles embedded in the glass matrix (see Figs. 1 and 2). The decrease of conductivity for the SC45 is thus the consequence of reduced intergranular amorphous region resulting from the formation of magnetite-based particles. The SC45-5Cu exhibits a semi-circle larger than that of SC45 yielding the lower conductivity of 1.0×10^{-7} S cm^{-1}. The resistive tendency for the SC45-5Cu could be caused by the intergranular amorphous region reduced by the growth of magnetite-based particles.

It is beneficial that the impedance data, coupled with FE-SEM, provides information on the fraction of magnetite-based particles embedded in the amorphous phases. A further large semi-circle is observed for the SC45-CuIE yielding the conductivity of 9.5×10^{-8} S cm^{-1}, which could be due, also in this case, to the reduced intergranular amorphous region. It is of interest that the fraction of magnetite-based particles for SC45-5Cu is smaller than that of SC45-CuIE despite larger magnetite crystallite (see Table I). We expect the coexistence of several kinds of Fe-based crystals along with Cu loading, by which the growth of magnetite-based particles for SC45-5Cu is interfered.

Table II lists the results of positron lifetime spectroscopy for (a) 45S5, (b) SC45, (c) SC45-5Cu, and (d) SC45-CuIE. The positron lifetime measurement for the 45S5 glass yields three components of positron lifetimes τ_1 ~194 ps, τ_2 ~238 ps, τ_3 ~740 ps with corresponding relative intensities I_1 ~27%, I_2 ~56%, and I_3 ~17%, respectively. The short-lived positron lifetimes of τ_1 correspond to the annihilation at the intrinsic open spaces in the amorphous matrix originating from the random packing of constituent atoms, which has been often observed for glass materials, as e. g., bulk metallic glasses [19]. The positron lifetime τ_2 is attributable to the trapped positrons at defects in the glass network, whereas the long-lived component of τ_3 ~740 ps arises from the pick-off annihilation of *ortho*-positronium (*o*-Ps) localized in the sub-nanoscale open spaces of the glasses. Similar results have been reported for soda-lime [37] and SiO_2 [38] glasses having open spaces with ~0.2 nm in size.

The SC45 exhibits two components of positron lifetimes τ_1 ~217 ps and τ_2 ~329 ps with corresponding relative intensities I_1 ~37% and I_2 ~63%, respectively. A disappearance of long-lived components is resultant of the

formation of a large fraction of magnetite-based particles thus reducing glass matrix as seen in the FE-SEM images (see Fig. 1).

Table II: Positron lifetimes and the corresponding relative intensities for (a) 45S5, (b) SC45, (c) SC45-5Cu, and (d) SC45-CuIE.

	τ_1 [ps]	I_1 [%]	τ_2 [ps]	I_2 [%]	τ_3 [ps]	I_3 [%]
(a) 45S5	194	27	238	56	740	17
(b) SC45	217	37	329	63	--	--
(c) SC45-5Cu	192	29	310	71	--	--
(d) SC45-CuIE	216	34	329	66	--	--

The short- and long-lived components are the consequence of positron annihilation inside the magnetite-based particles. We must underline that positron annihilation sites change from glass matrix to the magnetite-based particles for SC45. The positron lifetime τ_1 ~217 ps is longer than that in the bulk reported for magnetite natural crystal (~ 180 ps) [39], thus being ascribed to the annihilation in the vacancy-sized open spaces. The average positron diffusion length L_+ without any trapping centre is the order of ~ 100 nm for oxide ceramics [40]. As revealed by XRD experiments, the crystallite size of SC45 is 34 nm, which is by far smaller than the positron diffusion length in the oxide ceramics (see Table 1). Positrons implanted in the magnetite crystallites are thus expected to diffuse out and annihilate outside, leading to the conclusion that vacancy-sized open spaces are formed at the interfaces between magnetite crystallites. On the one hand, the positron lifetime τ_2 ~329 ps is similar to that of void (~ 300 ps) reported for magnetite natural crystal formed by sedimentation [39], thus corresponding to the void-like open spaces. The void-like open spaces could be located in the boundaries among the magnetite-based particles mainly created by lattice mismatching. Besides the present materials, positron annihilation at the interfaces and boundaries has been reported for several materials as e.g., nanocrystal-embedded Fe-based amorphous [41], and biogenic silica quartz [42,43].

Similarly to the case of SC45, two components of the positron lifetimes are obtained for the SC45-5Cu: the vacancy-sized open spaces in the interfaces between magnetite crystallites and void-like open spaces in the boundaries among the magnetite-based particles (see Table II). Both the positron lifetimes τ_1 ~192 ps and τ_2 ~310 ps are short in comparison with those of SC45, signifying the increases in local electron density around the positron annihilation sites upon Cu loading. This evidences the accommodation of Cu in the form of ions as Cu^{2+} into the crystallite interfaces in addition to the particle boundaries locally forming positive charges therein. The positive charges in the crystallite interfaces and particle boundaries attract electrons, by which the local electron densities increase reducing positron lifetimes τ_1 and τ_2. A similar phenomenon has been found at the grain boundaries for Gd-doped ceria electrolytes [23,24]. The relative intensity I_2 corresponding to void-like open spaces is ~71%, which is higher than that of SC45. This indicates that an introduction of Cu ions increases the concentration of boundaries among magnetite-based particles for SC45-5Cu. The positron lifetimes attributable to the vacancy-sized open spaces in the interfaces between magnetite crystallites and void-like open spaces in the boundaries among the magnetite-based particles are obtained for the SC45-CuIE sample as well (see Table II). In contrast to SC45-5Cu, the positron lifetimes τ_1 and τ_2 as well as the relative intensities I_1 and I_2 are similar to those of SC45, signifying that an introduction of Cu ions is less effective in two positron annihilation sites for SC45-CuIE. This demonstrates that Cu ions, introduced by means of an ion-exchange process, do not enter into both the crystallite interfaces and particle boundaries.

Figure 4 shows the results of CDB spectroscopy for (a) 45S5, (b) SC45, (c) SC45-5Cu, and (d) SC45-CuIE, where the ratio spectra normalized to that of pure Al are presented to highlight the differences among the spectral shape in the higher momentum core-electron region.

Unlike the 45S5 glass, the Doppler spectrum for the SC45 devitrified glass indicates a gentle slope above 20×10^{-3} m_0c, similar to that of pure Fe, as shown with a red solid line. This indicates that positrons probe core electrons of Fe atoms present in the vacancy-sized open spaces in the interfaces between magnetite crystallites and void-like open spaces in the boundaries among the magnetite-based particles.

The presence of Fe atoms around the positron annihilation sites is easily understandable because the large fraction of magnetite-based particles is formed for the SC45 (see FE-SEM images in Figure 1). The gradient at

high momentum core electron region for SC45-5Cu becomes steeper than that of SC45 as shown with a green solid line.

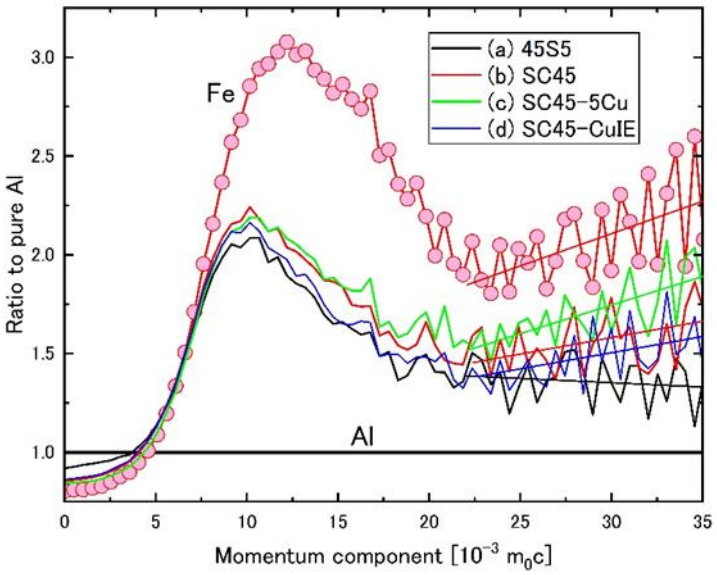

Figure 4: CDB spectra for (a) 45S5 (black solid line), (b) SC45 (red solid line), (c) SC45-5Cu (green solid line), and (d) SC45-CuIE (blue solid line) together with those of pure Al (Y=1) and Fe (red circles). All the spectra normalized to that of pure Al.

This implies that Cu ions are dispersed in the crystallite interfaces and particle boundaries contributing to positron annihilation together with Fe atoms. The presence of Cu ions in the crystallite interfaces and particle boundaries coincides with the reduced positron lifetimes (see Table II), which is more element specifically discussed using the correlation between valence and core electrons later. The gradient for the SC45-CuIE sample, in turn, gets gentle and rather similar to that of SC45, demonstrating fewer Cu ions around the positron annihilation sites, in agreement with the results of FE-SEM observation as well as positron lifetime spectroscopy.

Figure 5 shows the correlation between valence and core electron contribution, known as *S*-*W* correlation [44], taken from the momentum distribution of annihilation photons, which has been often employed for examining the chemical environment around positron annihilation sites [44].

The *S*-*W* correlation of 45S5 glass is located on the straight solid line with SiO_2 glass denoted as the SiO_2 line, indicating that the surrounding atoms of positron annihilation sites are similar to those of SiO_2 glass. The data

of SC45 are deviated from the SiO_2 line getting toward that of Fe, capturing the picture that positrons probe the electrons of Fe atoms in the crystallite interfaces and particle boundaries.

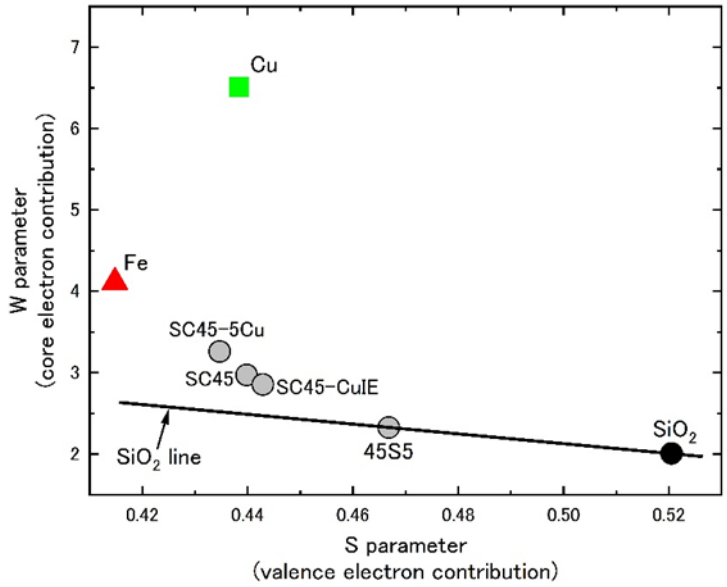

Figure 5: The correlation between *S* and *W* parameters taken from coincidence Doppler broadening spectra for 45S5, SC45, SC45-5Cu, and SC45-CuIE. All are plotted with black open circles. The data for SiO_2 (black solid circles) together with those for pure Fe (red solid triangles) and pure Cu (green solid squares) are presented for comparison. The solid line with the data of SiO_2 , denoted as the SiO_2 line, is drawn for guiding the eye.

The tendency of deviation becomes prominent getting toward that of Cu for the SC45-5Cu sample. The upward deviation from the SiO_2 line is the consequence of positron annihilation partially with the electrons of Cu in addition to Fe atom, again supporting the presence of Cu ions at the positron annihilation sites. The deviation from the SiO_2 line is less pronounced for SC45-CuIE, as Cu ions are not effectively introduced into the magnetite crystallite-crystallite interfaces and particle boundaries.

Figure 6 shows the results of FT-IR spectroscopy for (a) 45S5, (b) SC45, (c) SC45-5Cu, and (d) SC45-CuIE. The FT-IR spectrum of 45S5 glass exhibits peaks in a complex manner at wavenumbers of ~838 cm^{-1}, ~850 cm^{-1}, and ~920 cm^{-1}. These peaks are associated with Si-O-Si symmetric stretching vibration of SiO_4 tetrahedra possessing non-bridging oxygen in the nearest surrounding of Si atoms denoted as $Q^{(n)}$ species, which is often observed for glass materials with SiO_2 [45, 46]. The additional absorption peaks at ~1010 cm^{-1} can be attributed to Si-O-Si asymmetric stretching vibration of SiO_4 tetrahedral unit [47]. The distinct peaks of 45S5 glass caused by $Q^{(n)}$ species and SiO_4 asymmetric stretching vibration are smeared for the SC45, SC45-5Cu,

and SC45-CuIE devitrified glasses being dominant broad peaks of Si-O-Si stretching vibration, as the glass structure transforms to devitrified one.

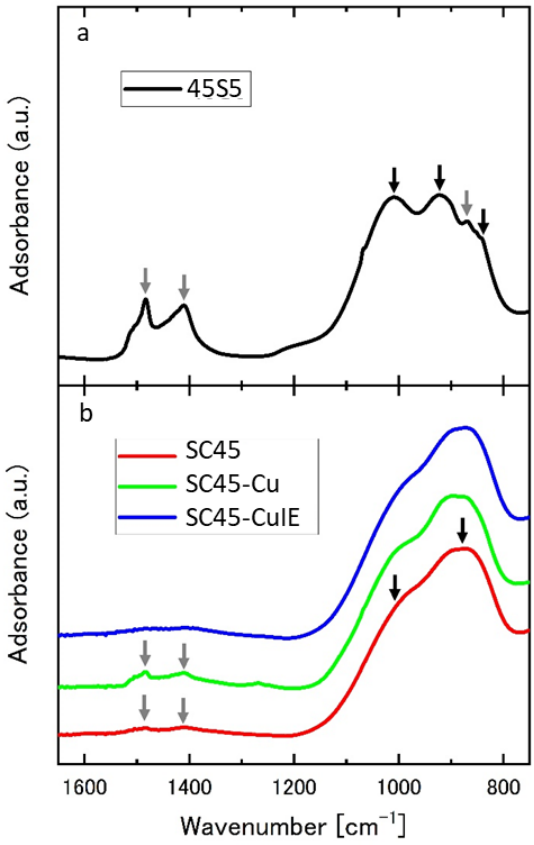

Figure 6: FT-IR spectra for 45S5 (black solid line), SC45 (red solid line), SC45-5Cu (green solid line), and SC45-CuIE (blue solid line). Adsorption peaks arising from SiO_4 tetrahedra and carbonate groups are indicated by black and grey arrows, respectively.

The absorption bands characteristic for asymmetric stretching vibration of carbonate appear at ~1410 cm^{-1} and ~1480 cm^{-1} for the 45S5 glass together with out-of-plane bending vibration at ~870 cm^{-1} (see Fig. 6 (a)), resultant from carbonate groups (CO_3^{2-}) [48, 49]. The formation of carbonate species could be caused by the reaction of Ca with CO_2 present in the air, due to the highly active surface of the amorphous region with tortuous porous structure [50, 51]. The peaks of carbonate groups weaken commonly for SC45, SC45-5Cu, and SC45-CuIE samples (see Fig. 6 (b)) basically due to the reduction of the amorphous region as revealed by electrochemical impedance spectroscopy. However, it was observed that the SC45 and SC45-5Cu samples exhibit significant peaks of carbonate species as indicated by arrows. The intensities of adsorption bands of carbonate species are more pronounced for SC45-5Cu than those of SC45, indicating that surface activity for three devitrified glasses is the order of SC45-5Cu, SC45, and SC45-CuIE (SC45-5Cu > SC45 > SC45-CuIE). It is

of interest that the surface activity observed for three devitrified glasses is not simply correlated with the fraction of intergranular amorphous region with open spaces. We reasonably infer that the interfacial structure with the void-like open spaces of magnetite-based particles identified by the present positron annihilation spectroscopy participates in the surface activity of devitrified glasses SC45-5Cu, SC45-CuIE, and SC45.

Based on the results of element-specific positron annihilation spectroscopy together with FE-SEM observation, XRD, and electro-chemical impedance spectroscopy, we discuss how Cu ions contribute to the formation of interfacial structures for magnetite-based particles in devitrified glasses providing the active surface area. The magnetite-based crystals observed by FE-SEM consist of elongated highly interpenetrated columns, formed by several octahedral crystals (size 0.5 - 5 μm), grown one over the other, with a vertex in common, with Maltese cross-type morphology. In the SC45-5Cu synthesized by the melt-quenching method, Cu elements are dispersed in the crystallite-crystallite interfaces and particle boundaries in the form of ions. Cu ions preferentially separate the magnetite-based particles during melt-quenching increasing the concentration of particle boundaries involved with the void-like open spaces. An interior surface of the void-like open spaces could be active as evidenced by the fact that the formation of carbonate species occurs through the reaction of Ca with CO_2 in air. In contrast to SC45-5Cu, fewer Cu ions are able to occupy both the crystallite-crystallite interfaces and particle boundaries for SC45-CuIE synthesized by the ion-exchanging method. Thus, the concentration of void-like open spaces in the crystal boundaries slightly decreases in comparison with those of SC45-5Cu, the surface activity being lower than that of SC45-5Cu. The present studies demonstrate that Cu ions dispersed into the magnetite-based crystal boundaries during melt-quenching play an important role not only in imparting an antibacterial effect but also in developing locally active surfaces.

Conclusions

The local atomic structure associated with surface activity, alternative to open spaces in the glass matrix, was explored for bioactive ferrimagnetic devitrified glasses doped with Cu elements by melt-quenching (SC45-5Cu) and ion-exchanging (SC45-CuIE). The results obtained for SC45-5Cu and SC45-CuIE were compared with

those of unloaded SC45 in addition to bioactive glass 45S5. FE-SEM observation showed the morphology of magnetite-based crystals embedded in the glass matrix for unloaded and Cu-loaded samples. Analyses of FE-SEM images indicated that the Cu species enters into the magnetite unit cell modifying its structure only for SC45-5Cu sample. The average sizes of magnetite crystallite for SC45-5Cu and SC45-CuIE are smaller than that of SC45, implying that Cu elements participate in interfering magnetite crystallites. Electro-chemical impedance spectroscopy for SC45-5Cu and SC45-CuIE indicated the resistive tendency higher than that of SC45 because the intergranular amorphous region with tortuous open spaces is reduced due to the growth of magnetite-based crystals. Element-specific positron annihilation spectroscopy for three devitrified glasses revealed the presence of vacancy-sized open spaces in the interfaces between magnetite crystallites as well as the void-like open spaces formed in the boundaries among the magnetite-based crystals. It is found that Cu elements located in the above interfacial structures are in the form of ion for SC45-5Cu and the void-like open spaces in the crystal boundaries is efficiently formed. An interior surface of the void-like open spaces could be active as evidenced from the results of FT-IR spectroscopy, where the formation of carbonate species occurs through the reaction of Ca with CO_2.

Funding

This work was partially supported by a Grant-in-Aid of the Japanese Ministry of Education, Science, Sports and Culture (Grant No. 22K03465).

References

[1] Fernandes HR, Gaddam A, Rebelo A, et al. Bioactive Glasses and Glass-Ceramics for Healthcare Applications in Bone Regeneration and Tissue Engineering. Materials (Basel). 2018;11(12):2530. doi: 10.3390/ma11122530

[2] Hench LL, Jones JR. Bioactive Glasses: Frontiers and Challenges. Front. Bioeng. Biotechnol. 2015; 3:194. doi: 10.3389/fbioe.2015.00194

[3] Lin I, Mauro JC, Kaur G. Chapter 10 - Bioactive Glasses for Cancer Therapy, Editor(s): Gurbinder Kaur, In Woodhead Publishing Series in Biomaterials, Biomedical, Therapeutic and Clinical Applications of Bioactive Glasses, Woodhead Publishing. 2019; p273-312. Doi: 10.1016/B978-0-08-102196-5.00010-0.

[4] Danewalia SS, Singh K. Bioactive glasses and glass-ceramics for hyperthermia treatment of cancer: state-of-art, challenges, and future perspectives. Mater Today Bio. 2021; 10:100100. Doi: 10.1016/j.mtbio.2021.100100.

[5] Miola M, Pakzad Y, Banijamali S, et al. Glass-ceramics for cancer treatment: So close, or yet so far?, Acta Biomaterialia 2019;83:55-70. Doi:10.1016/j.actbio.2018.11.013.

[6] Hoppe A, Güldal NS, Boccaccini AR. A review of the biological response to ionic dissolution products from bioactive glasses and glass-ceramics, Biomaterials 2011;32(11):2757-2774. Doi: 10.1016/j.biomaterials.2011.01.004.

[7] Pantulap U, Arango-Ospina M, Boccaccini AR. Bioactive glasses incorporating less-common ions to improve biological and physical properties. J Mater Sci: Mater Med 2022;33:3. Doi: 10.1007/s10856-021-06626-3

[8] Miola M, Massera J, Cochis A, et al. Tellurium: A new active element for innovative multifunctional bioactive glasses. Mater Sci Eng C Mater Biol Appl. 2021;123:111957. doi: 10.1016/j.msec.2021.111957

[9] Mouriño V, Cattalini JP, Boccaccini AR. Metallic ions as therapeutic agents in tissue engineering scaffolds: an overview of their biological applications and strategies for new developments. J R Soc Interface. 2012;9(68):401–419. Doi: 10.1098/rsif.2011.0611

[10] Hu X, Wang T, Li F, et al. Surface modifications of biomaterials in different applied fields. RSC Adv., 2023;13:20495–20511 Doi: 10.1039/D3RA02248J

[11] Miola M, Bertone E, Vernè E. In situ chemical and physical reduction of copper on bioactive glass surface, Applied Surface Science, 2019;495:143559. Doi: 10.1016/j.apsusc.2019.143559.

[12] Mathew R, Stevensson B, Tilocca A, et al.Toward a Rational Design of Bioactive Glasses with Optimal Structural Features: Composition–Structure Correlations Unveiled by solid-State NMR and MD Simulations Cite this: J. Phys. Chem. B 2014;118(3):833–844. Doi:10.1021/jp409652k

[13] Kapoor S, Brazete D, Pereira IC, et al. Impact of Transition Metal Ions on the Structure and Bioactivity of Alkali-Free Bioactive Glasses. J. Non-Cryst. Solids. 2019;506:98–108. Doi: 10.1016/j.jnoncrysol.2018.12.003

[14] Koohkan R, Hooshmand T, Tahriri M, et al. Synthesis, characterization and in vitro bioactivity of mesoporous copper silicate bioactive glasses. Ceram. Int. 2018;44:2390–2399. Doi: 10.1016/j.ceramint.2017.10.208.

[15] Miola M, Vernè E. Bioactive and Antibacterial Glass Powders Doped with Copper by Ion-Exchange in Aqueous Solutions. Materials 2016;9:405. Doi: 10.3390/ma9060405

[16] Wang H, Zhao S, Xiao W, et al. Influence of Cu doping in borosilicate bioactive glass and the properties of its derived scaffolds. Mater. Sci. Eng. C. 2016;58:194-203. https://doi.org/10.1016/j.msec.2015.08.027

[17] Stanić V, Variation in Properties of Bioactive Glasses After Surface Modification. In: Kaur, G. (eds) Clinical Applications of Biomaterials. Springer, Cham. 2017. https://doi.org/10.1007/978-3-319-56059-5_2

[18] Foroutan F, Kyffin BA, Nikolaou A, et al. Highly porous phosphate-based glasses for controlled delivery of antibacterial Cu ions prepared via sol-gel chemistry. RSC Adv. 2023;13:19662-19673. Doi: 10.1039/D3RA02958A

[19] Zhao Y, Li DD, Qu BY, et al. Anomalous packing state in Ce-Ga-Cu bulk metallic glasses. Intermetallics 2017;84:25-29,. Doi:10.1016/j.intermet.2016.12.017

[20] Li W, Li X, Guo D, et al. Atomic-scale structural evolution in amorphous Nd9Fe85B6 subjected to severe plastic deformation at room temperature. Applied Physics Letters 2009;94: 231904. Doi.org/10.1063/1.3152013

[21] Sato K. Study of salt precipitation in polymer electrolytes based on PEO and EMImTf ionic liquid. J. Phys. Chem. B 2018;122:7009-7014. Doi:10.1021/acs.jpcb.8b04429

[22] Yu RS, Ito K, Hirata K, et al. Positron annihilation study of defects and Si nanoprecipitation in sputter-deposited silicon oxide films. Chem. Phys. Lett. 2003;379:359-363. Doi: 10.1016/j.cplett.2003.08.056

[23] Sato K, Fujimoto K, Dai W, et al. Quantitative elucidation of Cs adsorption sites in clays: Toward sophisticated decontamination of radioactive C. The Journal of Physical Chemistry C 2016;120 (2):1270-1274. Doi: 10.1021/acs.jpcc.5b09350

[24] Sato K. Grain-boundary structures associated with ionic transport in Gd-doped ceria nanostructured electrolyte, J. Phys. Chem. C 2015;119:5734-5738. Doi: 10.1021/acs.jpcc.5b00155

[25] Sato K. Probing charge state distribution at grain boundaries varied with dopant concentration for ceria ceramics. J. Phys. Chem. C 2017;121:20407-20412. Doi: 10.1021/acs.jpcc.7b07978

[26] Bretcanu O, Verne` E, Coisson M, et al. Temperature effect on the magnetic properties of the coprecipitation derived ferrimagnetic glass-ceramics. J. Magn. Magn. Mater. 2006;300:412-417. Doi: 10.1016/j.jmmm.2005.05.030

[27] Bretcanu O, Vernè E, Coisson M, et al. Magnetic properties of the ferrimagnetic glass-ceramics for hyperthermia. J. Magn. Magn. Mater. 2006;305:529-533. Doi: 1016/j.jmmm.2006.02.264

[28] Vernè E, Miola M, Ferraris S, et al. Surface Activation of a Ferrimagnetic Glass–Ceramic for Antineoplastic Drugs Grafting. Advanced Engineering Materials 2010;12: B309-B319. Doi:10.1002/adem.200980082

[29] Bretcanu O, Miola M, Bianchi CL, et al. In vitro biocompatibility of a ferrimagnetic glass-ceramic for hyperthermia application. Materials Science and Engineering C 2017;73:778–787. Doi: 10.1016/j.msec.2016.12.105

[30] Miola M, Bruno M, Gerbaldo R, et al. Melt-derived copper-doped ferrimagnetic glass-ceramic for tumor treatment. Ceramics International 2021;47:31749–31755. Doi: 10.1016/j.ceramint.2021.08.056

[31] Miola M, Bruno M, Vernè E. Ferrimagnetic devitrified glass doped with copper by ion exchange: Microstructure, bioactivity and antibacterial properties. Ceramics International, 2024,in press. https://doi.org/10.1016/j.ceramint.2024.01.178.

[32] Larry LL, June Wilson H. An introduction to bioceramics. Singapore: Word Scientific, 1993; 620. Doi: 10.1142/p884

[33] Ito K, Oka T, Kobayashi Y, et al. Interlaboratory comparison of positron annihilation lifetime measurements for synthetic fused silica and polycarbonate. J. Appl. Phys. 2008;104:0261021-0261023. Doi: 10.1063/1.2957074

[34] Ito K, Oka T, Kobayashi, et al. Interlaboratory Comparison of Positron Annihilation Lifetime Measurements. Mater. Sci. Forum 2009; 607:248-250. Doi: 10.4028/www.scientific.net/MSF.607.248

[35] Morales AL, Velásquez AA, Urquijo JP, ey al. Synthesis and characterization of Cu2+ substituted magnetite. Hyperfine Interact., 2011; 203: 75-84 DOI: 10.1007/s10751-011-0349-x

[36] Rodrigues Gavinho S, Gonçalves Melo BM, Borges JP, et al. Thermal, Structural, Morphological and Electrical Characterization of Cerium-Containing 45S5 for Metal Implant Coatings. Coatings 2023;13(2):294. Doi: 10.3390/coatings13020294

[37] Sato K, Ito K. Rev. Sci. Improvement of the far-infrared optical property for glasses by plasma-assisted dispersion of fluorocarbon species into the shallow surface. Instrument 2022;92:063905. Doi:10.1063/5.0046936

[38] Sato K, Ohshima N. Evaluation Methodology of Diffusion Coefficient of Guest Substances Associated with Angstrom-Scale Open Spaces in Materials by Slow Positron Beam. N. Rev. Sci. Instrument 2020; 91: 0839071-0839075.

[39] Uhlmann K, Britton DT, Heger S. Investigation of goethite, hematite and magnetite, Materials Science Forum 1995;175-178: 225-228.

[40] Grynszpan RI, Saudé S, Mazerolles L, et al. Positron Depth Profiling in Ion-Implanted Zirconia Stabilized with Trivalent Cations. Radiat. Phys. Chem. 2007;76:333-336. Doi: 10.1016/j.radphyschem.2006.03.061

[41] Sato K, Murakami H, Sprengel W, et al. Nanocrystallization Mechanism of Amorphous Fe78B13Si9. Appl. Phys. Lett. 2009;94:1719041-1719043. Doi: 10.1063/1.3126041

[42] Sato K, Origin of Organism-Dependent Biogenic Silica Quartz Formation. J. Phys. Chem. B 2011;115 (49):14874-14877. Doi:10.1021/jp208720c

[43] Sato K, Fujimoto K, Nakata M, et al. Diffusion-Reaction of Water Molecules in Angstrom Pores as Basic Mechanism of Biogenic Quartz Formation. J. Phys. Chem. C 2011; 115:18131-18135. Doi: 10.1021/jp205299q

[44] K Sato, F Baier, AA Rempel, W Sprengel, HE Schaefer, Observation of high-temperature thermal vacancies in quasicrystals. Physical Review B 2003:68:214203. Doi: 10.1103/PhysRevB.68.214203

[45] Golovchak R, Thapar P, Ingram A, Savytskii D, et al. Influence of phase separation on the devitrification of 45S5 bioglass. Acta Biomaterialia 10, 2014, 4878-4886. Doi: 10.1016/j.actbio.2014.07.024

[46] Verma AS, Singh A, Kumar D, et al. Electro-mechanical and Polarization-Induced Antibacterial Response of 45S5 Bioglass–Sodium Potassium Niobate Piezoelectric Ceramic Composites. ACS Biomater. Sci. Eng. 2020;6:3055−3069. Doi: 10.1021/acsbiomaterials.0c00091

[47] Serra J, Gonzalez P, Liste S, et al. FTIR and XPS studies of bioactive silica-based glasses. J Non-Cryst Solids 2003;332:20–27. Doi: 10.1016/j.jnoncrysol.2003.09.013

[48] Paluszkiewicz C, Ślósarczyk A, Pijocha D, et al. Synthesis, structural properties and thermal stability of Mn-doped hydroxyapatite. J. Mol. Struct. 976, 2010, 301–309. Doi: 10.1016/j.molstruc.2010.04.001

[49] Kiminori S, Minori K. Origin of enhanced boric acid adsorption in light-burned magnesium oxide,J. Chem. Phys. 2020;153:1247041-1247048. Doi: 10.1063/5.0025455

[50] Cerruti M, Morterra C. Carbonate formation on bioactive glasses. Langmuir. 2004;20(15):6382-6388. Doi: 10.1021/la049723c.

[51] Du H, Williams CT, Ebner AD, et al. In Situ FTIR Spectroscopic Analysis of Carbonate Transformations during Adsorption and Desorption of CO_2 in K-Promoted HTlc. Chem Mater 2010;22:3519. Doi: 10.1021/cm100703e.